The Astrophysical Journal, 963:44 (9pp), 2024 March 1 https://doi.org/10.3847/1538-4357/ad22de
© 2024. The Author(s). Published by the American Astronomical Society.
OPEN ACCESS

COOL-LAMPS. VI. Lens Model and New Constraints on the Properties of COOL J1241+2219, a Bright $z = 5$ Lyman Break Galaxy and its $z = 1$ Cluster Lens

Maxwell Klein[1], Keren Sharon[1], Kate Napier[1], Michael D. Gladders[2,3], Gourav Khullar[4], Matthew Bayliss[5], Håkon Dahle[6], M. Riley Owens[5], Antony Stark[7], Sasha Brownsberger[8], Keunho J. Kim[5], Nicole Kuchta[1], Guillaume Mahler[9,10], Grace Smith[1], Ryan Walker[1], Katya Gozman[1], Michael N. Martinez[11], Owen S. Matthews Acuña[12], Kaiya Merz[13], Jorge A. Sanchez[14], Daniel J. Kavin Stein[2], Ezra O. Sukay[15], and Kiyan Tavangar[16]

[1] Department of Astronomy, University of Michigan, 1085 S. University Avenue, Ann Arbor, MI 48109, USA; kerens@umich.edu
[2] Department of Astronomy and Astrophysics, University of Chicago, 5640 South Ellis Avenue, Chicago, IL 60637, USA
[3] Kavli Institute for Cosmological Physics, University of Chicago, Chicago, IL 60637, USA
[4] Department of Physics and Astronomy, and PITT PACC, University of Pittsburgh, Pittsburgh, PA 15260, USA
[5] Department of Physics, University of Cincinnati, Cincinnati, OH 45221, USA
[6] Institute of Theoretical Astrophysics, University of Oslo, P.O. Box 1029, Blindern, NO-0315 Oslo, Norway
[7] Center for Astrophysics | Harvard & Smithsonian, Observatory Building E, 60 Garden Street, Cambridge, MA 02138, USA
[8] Department of Physics, Harvard University, 17 Oxford Street, Cambridge, MA 02138, USA
[9] Centre for Extragalactic Astronomy, Durham University, South Road, Durham DH1 3LE, UK
[10] Institute for Computational Cosmology, Durham University, South Road, Durham DH1 3LE, UK
[11] Department of Physics, University of Wisconsin-Madison, 1150 University Avenue, Madison, WI 53706, USA
[12] Department of Astronomy, University of Wisconsin-Madison, 475 N Charter Street, Madison, WI 53706, USA
[13] Space Telescope Science Institute, 3700 San Martin Drive, Baltimore, MD 21218, USA
[14] School Of Earth and Space Exploration, 781 Terrace Mall, Tempe, AZ 85287, USA
[15] Department of Physics and Astronomy, Johns Hopkins University, 3400 North Charles Street, Baltimore, MD 21218, USA
[16] Department of Astronomy, Columbia University, 550 West 120th Street, New York, NY 10027, USA
Received 2023 November 4; revised 2024 January 18; accepted 2024 January 24; published 2024 February 28

Abstract

We present a strong lensing analysis of COOL J1241+2219, the brightest known gravitationally lensed galaxy at $z \geqslant 5$, based on new multiband Hubble Space Telescope (HST) imaging data. The lensed galaxy has a redshift of $z = 5.043$, placing it shortly after the end of the "Epoch of Reionization," and an AB magnitude $z_{\rm AB} = 20.47$ mag (Khullar et al.). As such, it serves as a touchstone for future research of that epoch. The high spatial resolution of HST reveals internal structure in the giant arc, from which we identify 15 constraints and construct a robust lens model. We use the lens model to extract the cluster mass and lensing magnification. We find that the mass enclosed within the Einstein radius of the $z = 1.001$ cluster lens is $M(<5\farcs77) = 1.079^{+0.023}_{-0.007} \times 10^{13} M_\odot$, significantly lower than other known strong lensing clusters at its redshift. The average magnification of the giant arc is $\langle \mu_{\rm arc} \rangle = 76^{+40}_{-20}$, a factor of $2.4^{+1.4}_{-0.7}$ greater than previously estimated from ground-based data; the flux-weighted average magnification is $\langle \mu_{\rm arc} \rangle = 92^{+37}_{-31}$. We update the current measurements of the stellar mass and star formation rate (SFR) of the source for the revised magnification to $\log(M_\star/M_\odot) = 9.7 \pm 0.3$ and ${\rm SFR} = 10.3^{+7.0}_{-4.4}\ M_\odot\ {\rm yr}^{-1}$, respectively. The powerful lensing magnification acting upon COOL J1241+2219 resolves the source and enables future studies of the properties of its star formation on a clump-by-clump basis. The lensing analysis presented here will support upcoming multiwavelength characterization with HST and JWST data of the stellar mass assembly and physical properties of this high-redshift lensed galaxy.

Unified Astronomy Thesaurus concepts: Strong gravitational lensing (1643); Gravitational lensing (670); Galaxy clusters (584); Galaxy formation (595)

1. Introduction

Gravitational lensing is nature's telescope: massive foreground structures, such as galaxy clusters, magnify and distort background galaxies, greatly increasing the angular extent of the source and the number of photons that reach the observer. Using observational evidence of gravitational lensing, we can reconstruct the gravitational potential of the lens and study the mass distribution of the foreground cluster and the physical properties of the distant galaxies that the cluster lenses. Strong gravitational lensing can greatly magnify galaxies that would otherwise be too dim to study, allowing for spatial resolution of hundreds or even tens of parsecs (e.g., Johnson et al. 2017a, 2017b; Cornachione et al. 2018; Claeyssens et al. 2023; Vanzella et al. 2023; Welch et al. 2023). With a robust lens model, the lensed galaxy can be delensed into a high-resolution projection of the background galaxy in the source plane. These fortuitous alignments of background galaxies and strong gravitational lenses give us the best possible glimpse into the distant Universe, providing detailed information on the physical properties of galaxies. While wide surveys like the Sloan Digital Sky Survey (SDSS; Ahumada et al. 2020) have identified many bright $z < 3$ lensed galaxies, such discoveries are rare at higher redshifts (Franx et al. 1997; Soifer et al. 1998; Frye et al. 2002; Gladders et al. 2002; Kubo et al. 2010; Bayliss et al. 2011; Stark et al. 2013).

Original content from this work may be used under the terms of the Creative Commons Attribution 4.0 licence. Any further distribution of this work must maintain attribution to the author(s) and the title of the work, journal citation and DOI.

COOL J1241+2219 (hereafter COOL J1241), is a bright, strongly lensed galaxy at $z = 5.043$, lensed by a galaxy cluster at $z = 1.001$. It was discovered by the ChicagO Optically-selected Lenses — Located At the Margins of Public Surveys (COOL-LAMPS) collaboration (Khullar et al. 2021b; hereafter K21). The program seeks to find strong lensing systems in sky surveys for follow-up observation and analysis. The discovery, and an initial analysis based on ground-based data, are reported in K21. Remarkably, COOL J1241 has an AB magnitude $z = 20.47$ mag; it is ∼5–13 times brighter and 2%–4% farther away than the brightest known lensed galaxies at $z \sim 5$ (Franx et al. 1997; Soifer et al. 1998; Frye et al. 2002; Gladders et al. 2002). COOL J1241 is one of the rarest and most fortunate examples of strong gravitational lensing.

By the redshift of COOL J1241, $z \sim 5$, the "Epoch of Reionization" had ended (e.g., Fan et al. 2006; see Gnedin & Madau 2022; Robertson 2022 for recent reviews) and the cosmic star formation rate (SFR) was rapidly increasing. K21 found that COOL J1241 has a stellar mass similar to that of the Milky Way and a SFR that is 1 to 2 orders of magnitude higher. However, COOL J1241 is unlike other known galaxies within this epoch due to its lower relative dust content and SFR (K21). This points to a star formation history with potentially significant mass assembly in the recent past (for it to have formed its stellar mass so rapidly); although how many epochs of bursty star formation occurred, or how long these star-forming episodes were, are unclear with extant data. The effect of dust-enshrouded star formation on the total SFR in this epoch is still not understood (Casey et al. 2019; Mowla et al. 2022; Claeyssens et al. 2023). Upcoming JWST data (JWST Cycle 1, ID 2566; PI: Khullar; Khullar et al. 2021a) will allow for a deconstruction of the complete star formation history and characterization of mass assembly in this system.

K21 constructed a lens model of this system using ground-based data in the J and H bands from the FourStar Infrared Camera (Persson et al. 2008) on the Magellan/Baade telescope in Chile, as well as in the g, r, i, and z bands from the Parallel Imager for Southern Cosmology Observations (Stalder et al. 2014). As is the case with ground-based data, the resolution was low. Nevertheless, the data still enabled a rudimentary lens model and mass approximation for the galaxy cluster, and a preliminary source analysis. With the Hubble Space Telescope (HST), a higher spatial resolution provides better lensing constraints, leading to a more robust mass and magnification measurement (e.g., Sharon et al. 2012; Sukay et al. 2022; Zhuang et al. 2023).

The goal of this paper is to present an improved, space-based lens model that allows us to extract more accurate and precise information about both the lens and the source, and create a stepping stone toward future study with forthcoming JWST data. This paper is structured as follows. In Section 2, we present the HST imaging and data reduction. In Section 3, we present the methods used to generate the lens model, measure masses and magnifications, and obtain their uncertainties. In Section 4, we present the results of the model, namely the mass and magnification maps, as well as the magnification measurements. Finally, in Section 5, we use our results to revise the findings of K21, and discuss the significance of the results in the context of high-redshift galaxies and strong lensing galaxy clusters at $z \gtrsim 1$.

We assume a flat Universe with parameters $H_0 = 70\,\mathrm{km\,s^{-1}\,Mpc^{-1}}$, $\Omega_m = 0.3$, and $\Omega_\Lambda = 0.7$. Magnitudes are presented in the AB system. The spectroscopically measured cluster and source redshifts are $z_{\rm cluster} = 1.001$ and $z_{\rm source} = 5.043$, respectively, which correspond to 8.0106 and 6.2561 kpc per arcsec in this cosmology.

2. Data

The data were collected as part of a joint Very Large Array (VLA) and HST program (VLA/2020-07-025, HST GO-16484, PI: A. Stark; Stark et al. 2020). The data include three orbits of HST imaging split between four broadband filters: half an orbit each for two WFC3/IR bands, F110W (1012 s) and F160W (1212 s) observed on 2022 January 4, and one orbit in each of two Advanced Camera for Surveys (ACS) bands, F814W and F606W (2080 s each) observed on 2021 December 10. The ACS data were obtained with a simple four-point dither sequence using the standard `ACS-WFC-DITHER-BOX`. Because the observed lensing configuration suggested that a few tens of arcseconds around the lens center are of most interest, there was no need to fill the chip gap. The chip 2 pointing aperture was used in order to avoid a star on the field edges that could enter the field of view at some roll angles.

The orbit packing of the single WFC3/IR orbit was guided by a goal of obtaining a minimum of four dithered images per filter for adequate point-spread function sampling. Four images per filter were obtained with the `WFC3-IR-DITHER-BOX-MIN` pattern, using `NSAMP` = 11 and `SPARS25` for F110W and `NSAMP` = 7 and `SPARS50` for F160W, resulting in a slightly longer observing time in F160W due to buffer time constraints.

We reduced the data using the DrizzlePac Python package[17] as follows. We obtained the individual preprocessed frames from the MAST archive shortly after data acquisition. We used `AstroDrizzle` to coadd the subexposures of each filter, using a Gaussian kernel drop size of 0.8 for the ACS images and 1.0 for WFC3. For the WFC3/IR data, we applied a secondary correction of the IR blobs using a model-based flat-fielding technique (Sharon et al. 2020) prior to combining the individual IR exposures. We used `TweakReg` to match the world coordinate system solution of the imaging data that were obtained in different epochs (i.e., the WFC3 and ACS data). We then propagated the solution back to the individual frames using `TweakBack`, and redrizzled to obtain the final set of charge-transfer-efficiency-corrected, cosmic-ray- and bad-pixel-rejected images, with a common reference frame and a pixel scale of $0\farcs03$ pixel^{-1}. A representative HST (F160W, F814W, and F606W) color image of the strong lensing region of COOL J1241 is shown in Figure 1.

3. Methods

3.1. Lensing Evidence

The lensing analysis of K21 assumed that the lensing configuration of COOL J1241 is a common three-image arc with a counterimage, and that high magnification near the critical curve is responsible for the high brightness of a clump near the center of the giant arc. As we describe below, the ground-based imaging used for their analysis had insufficient resolution to reveal the complexity of the system.

In the common three-image arc configuration, three near-complete images of the source merge to form a giant arc (e.g., SDSS J1110+6459, Johnson et al. 2017a; SPT-CL J2011

[17] http://www.stsci.edu/scientific-community/software/drizzlepac.html

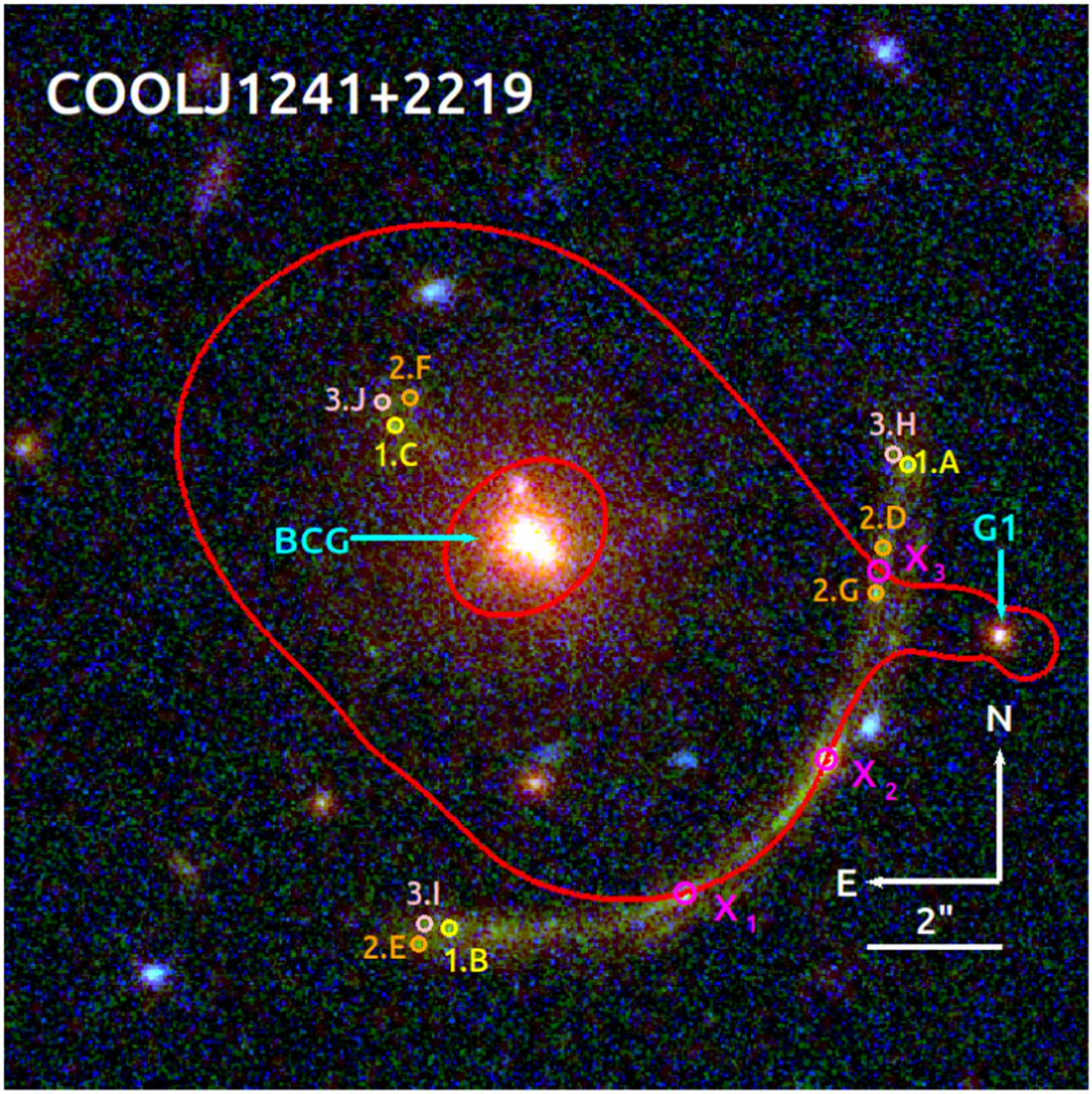

Figure 1. HST imaging of COOL J1241, rendered from F160W (red), F814W (green), and F606W (blue). The best-fit lens model is overplotted. The solid red lines denote the critical curve for a source at $z = 5.043$. The cyan arrows point to the brightest cluster galaxy (BCG), and a galaxy-scale halo (G1) whose parameters were optimized by the model. Magenta "X" symbols mark the locations of critical curve constraints (X_2 was carried over from K21, and X_2 was constraint 1.2 in K21). Multiple images that were used to constrain the lens model are labeled with circles and letters, and color coded according to their source identification (see Table 1).

−5228, Collett et al. 2017) with the critical curve crossing the arc in two places, defining clear mirror symmetry on its opposite sides. If a counterimage forms (in configurations other than a "naked cusp"), it is usually a less magnified, complete image. The high resolution of our shallow HST imaging reveals the clumpiness of the source, and makes it clear that the lensing configuration of COOL J1241 deviates from the common three-image arc configuration. We identified several star-forming clumps along the arc and used their relative surface brightnesses and slight variations in color to match and identify them as multiple image instances of unique regions in the source galaxy. We label the clumps in Figure 1, and their coordinates are listed in Table 1. We find that similar to the common three-image arc configuration described above, COOL J1241 has an image of the source in each end of its giant arc, which match the complete, less magnified counterimage near the BCG. However, most of the middle segment of the arc is not easily mapped to the other images. It appears to contain two bright clumps that do not match other clumps in terms of surface brightness and morphology. The counterimage lacks a clump with such a high surface brightness. The only likely explanation of these bright clumps along the arc is that they are a result of extreme magnification, caused by very close proximity to the source-plane caustic (aka, "caustic crossing"), as was concluded by K21 for the brightest clump. Such scenarios have been reported in the literature for other systems (e.g., Welch et al. 2022a, 2022b; Diego et al. 2022; Meena et al. 2023). In the case of COOL J1241, it is likely that the

Table 1
Coordinate Locations of Constraints and the Corresponding Magnifications, as Derived from the Best-fit Model

Source	Image	R.A. (J2000) (deg)	Decl. (J2000) (deg)	μ
1	A	190.3755783	22.3297457	33^{+17}_{-8}
1	B	190.3755783	22.3278230	17^{+9}_{-5}
1	C	190.3735237	22.3299101	6^{+3}_{-2}
2	D	190.3736331	22.3294010	275^{+416}_{-139}
2	E	190.3757184	22.3277581	14^{+8}_{-4}
2	F	190.3757558	22.3300264	6^{+4}_{-2}
2	G	190.3736638	22.3292139	179^{+313}_{-48}
3	H	190.3758224	22.3297899	35^{+17}_{-9}
3	I	190.3735880	22.3300055	16^{+9}_{-4}
3	J	190.3758824	22.3278459	7^{+4}_{-2}
Crit	X_1	190.3745218	22.3279684	⋯
Crit	X_2	190.3738858	22.3285245	⋯
Crit	X_3	190.3736529	22.3293070	⋯

Note. Uncertainties are inferred from Markov Chain Monte Carlo (MCMC) sampling of the parameter space and represent the difference between the best-fit value and the 16th and 84th percentiles. The critical curves are constrained to pass within 0.″05 of the listed coordinate.

central portion of the arc forms along the critical curve like a segment of an Einstein ring (e.g., the "Cosmic Horseshoe;" Bellagamba et al. 2017).

K21 used as constraints three brightness peaks along the arc, under the assumption that these are the core of the lensed galaxy, matched to the center of the candidate counterimage. In addition, they used two regions with similar surface brightness marking the edges of the star-forming clump that was assumed to be merging on the critical curve.

With the new high-resolution HST imaging, we find that the brightest regions of the giant arc formed as a result of high magnification or multiplicity rather than being a dominant core of the source galaxy. For the brightest of the clumps, our analysis concurs with the assumption of K21 that the brightest clump sits on top of the critical curve. Conversely, the peak brightness in the north segment of the arc, identified as 1.3 in K21, is actually resolved in the HST data into two images of one star-forming clump separated by 0.″7, with mirror symmetry (labeled 2.D and 2.G in Figure 1 and Table 1). To form these two images requires that a critical curve crosses the arc north of its assumed crossing in the K21 model, likely due to a contribution from a cluster-member galaxy ∼1.″7 west of the arc that complicates the lensing potential in that region.

Image 1.2 of K21 is a compact clump whose brightness and morphology are not matched by any other clump, and therefore could also be associated with caustic crossing. Finally, the regions north and south of the brightest clump are not symmetrical, providing evidence that the critical curve is not perpendicular to the arc at this location. We describe the new lensing constraints below.

Our model uses as constraints three unique star-forming clumps within the source galaxy of COOL J1241, and three critical curve constraints on the giant arc. The clumps were identified based on similarities in surface brightness and color. Only the most secure clump identifications were used as constraints. We did not include constraints from the middle section of the arc because these were hard to identify robustly as multiple images of the clumps at the north and south ends of the arc and the counterimage. This region is primarily constrained by forcing the critical curve to pass through points on the arc as determined by the lensing symmetry.

The critical curve constraint X_2 marks the brightest part of the giant arc, a constraint that was carried over from K21. X_3 to the north of the arc forces the model to form the mirror image geometry of 2.D and 2.G. Finally, X_1 accounts for a bright clump that does not map properly to other images. The most likely interpretation is that a region of the background galaxy is located almost directly under the lensing caustic, resulting in a highly magnified image of that region. Adding this constraint to the model resulted in better agreement between the predicted and observed lensing constraints, i.e., better image-plane rms. In Table 1, we list the coordinates, group, and image ID of each of the identified image constraints, and the location of the critical curve constraints in arcseconds relative to the BCG.

While the HST data resulted in several precise constraints along the giant arc and its counterimage, which improved upon the constraints of K21, the data did not reveal any new lensed galaxies. We detected some blue sources in the field, but were unable to confirm them robustly as strongly lensed nor obtain a spectroscopic redshift for them. Additionally, the location of some of these candidates, whose projected distance from the BCG placed them farther than the radius of the main arc, implies that they should be at a higher redshift than COOL J1241. Such a high redshift is ruled out by the blue color of these candidates. We, therefore, conclude that these sources are unlikely strongly lensed and exclude them from our analysis.

The lack of constraints from multiple source planes is a weakness of the model, as its leverage over the inner slope of the mass distribution is limited, resulting in systematic uncertainties that are not well captured by the error analysis (e.g., Johnson & Sharon 2016).

3.2. Lens Modeling

We computed the model using the `Lenstool` (Jullo et al. 2007) software, following the procedure described in Sharon et al. (2020). `Lenstool` assumes a parametric model of the projected mass distribution of the cluster lens, and uses MCMC sampling of the parameter space to find the model that results in the smallest image-plane rms scatter between the observed images and those predicted by the lens model. The cluster lens was modeled as a linear combination of mass halos representing the dark matter distribution of the cluster and its large-scale structure as well as individual cluster-member galaxies. Each halo was assumed to have a pseudoisothermal ellipsoidal mass distribution (dPIE; also referred to as PIEMD in the literature; Elíasdóttir et al. 2007; Jullo et al. 2007) with seven parameters: position (x, y), ellipticity (e), position angle (θ), core and cut radii ($r_{\rm core}$, $r_{\rm cut}$), and effective velocity dispersion (σ). Cluster-member galaxies were selected photometrically, based on their color with respect to the red sequence (Gladders & Yee 2000) in a color–magnitude diagram. We used F814W − F110W versus F110W, which provides good sampling of the 4000 Å break in the spectral energy distribution (SED) of quiescent galaxies at the cluster redshift. The cluster-member galaxies were also parameterized as dPIE halos, with positional parameters (x, y, θ, and e) fixed to their light distribution as measured with Source Extractor (Bertin & Arnouts 1996) and

Table 2
Best-fit Lens-model Parameters

No.	Component	ΔR.A (arcsec)	ΔDecl (arcsec)	e	θ (deg)	$r_{\rm core}$ (kpc)	$r_{\rm cut}$ (kpc)	σ_0 (km s^{-1})
1	Cluster	$-0.62^{+4.21}_{-1.92}$	$-2.51^{+4.10}_{-1.37}$	$0.18^{+0.06}_{-0.10}$	131^{+3}_{-9}	133^{+66}_{-51}	[1500]	985^{+262}_{-222}
2	BCG	[0.0]	[0.0]	$0.07^{+0.23}_{-0.02}$	140^{+15}_{-23}	$4.5^{+0.3}_{-4.4}$	50^{+47}_{-25}	298^{+2}_{-86}
3	G1	[−7.078359]	[−1.463040]	[0.033]	[−81.44]	[0.029]	[9.5]	95 ± 26
	L^* galaxy	…	…	…	…	…	$10.7^{+63.5}_{-6.3}$	137^{+8}_{-80}

Note. Coordinates are tabulated in arcseconds from the center of the BCG, [R.A., decl.] = [190.3752375, 22.3294502]. All the mass components were parameterized as dPIE (see Section 3), with ellipticity expressed as $e = (a^2 - b^2)/(a^2 + b^2)$. θ is measured north of west. Statistical uncertainties were inferred from the MCMC optimization and correspond to a 95% confidence interval. Parameters in square brackets were not optimized. The location and the ellipticity of cluster galaxies were kept fixed according to their light distribution, and the other parameters were determined through scaling relations (see text). The image-plane rms of the best-fit model is 0.″16.

their slope parameters and normalization scaled to their measured magnitudes in F110W using scaling relations as described in Limousin et al. (2005).

The best-fit solution of the lens plane used three halos with free parameters: a cluster-scale halo representing the cluster, and two galaxy-scale halos that were decoupled from the cluster-member catalog. These cluster-member galaxies were the BCG, which is not expected to follow the same scaling relations as other cluster-member galaxies, and the galaxy labeled G1 in Figure 1, because of its proximity to the giant arc. The positional parameters of these galaxies were fixed, but some or all of their slope parameters were allowed to vary and the best-fit solution was identified by the lens modeling process.

4. Results

The lens plane is well described by a dominant dark matter halo, representing the cluster-scale mass distribution, supplemented with galaxy-scale halos representing the BCG and cluster-member galaxies. Contribution to the lensing potential from galaxy G1 was required in order to reproduce the lensing configuration of the star-forming clumps observed in the giant arc. The normalization parameter σ of G1 was optimized individually, in order to add flexibility to the lens model and avoid biasing the scaling relation parameters toward a solution that is primarily driven by one galaxy. The model predicts a demagnified fifth image of the source behind the BCG, 5–6 mag fainter than the observed arcs. Given its magnification, it is not expected to be visible in the data. The model has 14 free parameters and 24 constraints, and results in an rms scatter of 0.″16 for predicted images in the image plane.

In Table 2 we tabulate the best-fit lens-model parameters and their uncertainties, as determined from the MCMC sampling of the parameter space. Figure 1 displays the lensing constraints and the critical curves for a source at $z = 5.043$ derived from the best-fit lens model.

Figure 2 shows the best-fit magnification map for a source at $z = 5.043$. Representative magnification values at the locations of the lensing constraints are presented in Table 1. The errors were estimated by generating 100 models sampled from the MCMC chain and finding the 16th and 84th percentiles of the magnification at each coordinate. The uncertainties represent statistical modeling errors, and do not take into account systematic uncertainties. As expected, regions in close proximity to the critical curve have higher magnification and uncertainty.

A calculation of the average magnification of the entire arc is complicated by the proximity of the arc to the critical curve,

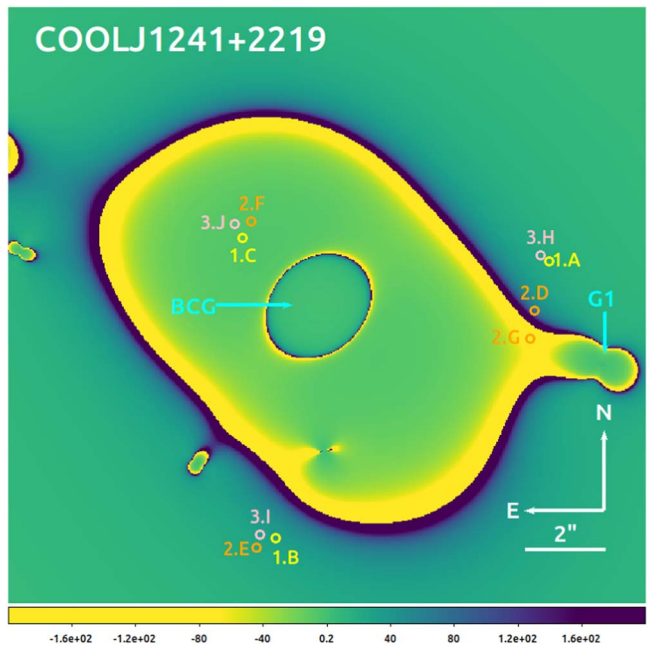

Figure 2. Magnification map of the galaxy cluster, centered on the BCG, for a source at $z = 5.043$. The color scale indicates magnification, with positive and negative values having opposite lensing parity. The field of view and labels are the same as Figure 1.

which marks regions in the image plane where a point source would theoretically have infinite magnification. To avoid numerical effects near the critical curve, we calculated the magnification by comparing the image-plane area to the source-plane area as follows. We traced the arc with an aperture of width 0.″8; using the deflection matrices α of the best-fit model and the 100 models sampled from the MCMC, we ray traced the aperture to the source plane using the lens equation $\beta = \theta - \alpha(\theta)$, where β is the source position, θ is the image position, and α is the lensing deflection at position θ. We then used the ratio of the image-plane area to the source-plane area to calculate the average magnification and its uncertainty. The same approach was used by K21; we compare our magnification measurements in Section 5. The average magnification of the entire giant arc is $\langle \mu_{\rm arc} \rangle = 76^{+40}_{-20}$, and the counterimage is magnified by $\langle \mu_{c.i.} \rangle = 6.6^{+2.6}_{-2.2}$.

The mean projected distance between the giant arc and the BCG is 5.″77. The mass enclosed within this radius, from our lensing analysis, is $M(<5.''77) = 1.079^{+0.023}_{-0.007} \times 10^{13} M_\odot$. The analytical expression for the mass enclosed within the Einstein radius of a spherically symmetrical lens is

$M(<\theta_E) = \Sigma_{cr}\pi[D_L\theta_E]^2 = 1.17\times10^{13}M_\odot$ for an Einstein radius of $\theta_E = 5.''77$, corresponding to 46.2 kpc at the lens redshift. In this equation, Σ_{cr} is the critical density for lensing and D_L is the angular diameter distance to the lens (see, e.g., Kneib & Natarajan 2011). Using numerical simulations, Remolina González et al. (2020) showed that the $M(<\theta_E)$ analytical mass estimate for a system with a similar lensing configuration as COOL J1241 (azimuthal arc coverage $\sim 40\%$) is biased high by 10% and has a 9% uncertainty after correcting this bias. This bias is primarily the result of mass distribution ellipticity deviating from the assumed spherical symmetry. Applying this correction to the analytical estimate results in $M_{corr}(<\theta_E) = 1.07\pm0.11\times10^{13}\ M_\odot$. We report that our lens-model-based mass measurement and the analytical estimate for $M(<\theta_E)$ are consistent within the uncertainties.

5. Discussion

The strong gravitational lensing model for COOL J1241 facilitates the ongoing and future investigation of the lensed $z = 5.043$ background galaxy and its intrinsic properties, such as SFR, stellar mass, morphology, and the sizes of the star-forming clumps.

5.1. Comparison to the Previously Published Lensing Analysis of COOL J1241+2219

One of the primary results of this paper is the significant difference between our lens model and the K21 model. Due to the ground-based seeing limitations, the data used by K21 did not have the resolution needed to properly resolve the clumpiness of the arc properly. As a result, their ability to interpret the lensing configuration correctly was reduced, and the low number of available constraints limited the number of free parameters and complexity of the lens model. Section 3.1 details the differences in the modeling assumptions and lensing constraints between the two models. Because the critical curve was constrained to intersect the arc in three places, the new model predicts that a large portion of the arc forms along the critical curve, resembling a segment of an Einstein ring. As a result, our measurement of the average magnification of the arc is significantly higher than the previous model, $\langle\mu\rangle = 76^{+40}_{-20}$ versus $\langle\mu\rangle = 32^{+8}_{-5}$. This difference, of a factor of $2.4^{+1.4}_{-0.7}$ higher, propagates to the measurements of the intrinsic properties of the lensed galaxy as we describe in Section 5.3. This is perhaps an anecdotal indication of a global concern with the inaccuracy of ground-based data for lensing models. It is also notable that our model results in a higher fractional statistical uncertainty on the magnification, which is counter-intuitive to what is expected from models using space-based resolution. The high statistical uncertainty is due to the proximity of a large portion of the arc to the critical curve, where the uncertainties are high. A future analysis of JWST NIRCam data (JWST ID 2566; Khullar et al. 2021a) may reveal infrared color variations that can be used to increase the constraining power of the lensing evidence, reduce the magnification uncertainties, and improve the accuracy of the lens model.

5.2. Comparison to Strong Lensing Clusters at z $\gtrsim$ 1

Attempting to compare our mass estimate of the foreground cluster that lenses COOL J1241 to that of other $z \gtrsim 1$ clusters is not straightforward. While numerous clusters and protoclusters are now known in this redshift bin, an estimate of their masses usually comes from mass proxies such as X-ray emission, the Sunyaev–Zel'dovich (SZ) effect, or from weak lensing. As such, most mass estimates available in the literature are reported for r_{200c} or r_{500c}, which represent the radius from the center of the cluster where the density is, respectively, 200 or 500 times the critical density of the Universe at the cluster redshift (or similarly, 200 times the mean density, for $M_{200,m}$). Given that our mass measurement relies solely on constraints from the arc and its counterimage at the innermost core of the cluster, we cannot reliably extrapolate it beyond a few tens of arcseconds in projection from the BCG. The aforementioned mass proxies lack the spatial resolution needed to measure the mass at the small cluster-centric radii that strong lensing probes. Since a mass comparison to the general population of clusters would be unreliable, we situate the strong lensing inferred mass we measured at the core of the cluster lens COOL J1241 in the context of other known strong lensing clusters at $z \gtrsim 1$.

To date, there are only a handful of strong lensing clusters at $z > 1$ in the literature, with cluster mass estimates using a variety of techniques and at different radii. SPT-CL J0356−5337, a $z = 1.0359$ cluster and a major merger candidate, has a projected mass density of $M(<500\text{ kpc}) = 4.0\pm0.8\times10^{14}\,M_\odot$ (Mahler et al. 2020) inferred from strong lensing analysis, and $M_{500c} = 3.59^{+0.59}_{-0.66}\times10^{14}\,M_\odot$ (Bocquet et al. 2019) from the SZ effect. SPT-CL J0546−5345 at $z = 1.067$, has a total mass of $M_{200} = 1.0^{+0.6}_{-0.4}\times10^{15}M_\odot$, measured by Brodwin et al. (2010) by combining optical, dynamical, X-ray, and SZ mass proxies. Andersson et al. (2011) reported $M_{500} = 5.3\pm1.3\times10^{14}\,M_\odot$ for this cluster. IDCS J1426.5+3508 is at $z = 1.75$ (Gonzalez et al. 2012) with a Chandra X-ray mass measurement of $M_{500,L_x} = 3.3\pm0.1\times10^{14}\,M_\odot$ (Stanford et al. 2012) and a SZ mass measurement of $M_{200,m} = 4.3\pm1.1\times10^{14}\,M_\odot$ (Brodwin et al. 2012). SPT-CL J2011−5228 is at $z = 1.064$, with $M_{500} = 2.25\pm0.89\times10^{14}\,M_\odot$ (Reichardt et al. 2013), measured from the SZ effect. Collett et al. (2017) report a mass within an Einstein radius of $\theta_E = 14.''01$ of $M_E \sim 1.6\times10^{14}\,M_\odot$ from a strong lensing analysis of this cluster. Finally, SPT-CL J0205−5829 at $z = 1.322$ has a mass estimate of $M_{500} = 4.8\pm0.8\times10^{14}\,M_\odot$ from a combined X-ray and SZ analysis (Stalder et al. 2013; Bleem et al. 2015).

As noted above, absent mass proxies at larger cluster-centric radii, an extrapolation of the strong lensing inferred mass of the cluster lens COOL J1241 to R_{200}, R_{500}, or even to a few hundred kiloparsecs, is highly inaccurate. We therefore opted to compare its well-constrained inner core mass to that of the other lensing clusters in its redshift bin, listed above. The projected mass density within the Einstein radius of a strong lensing cluster is well constrained from the strong lensing evidence alone, even without a detailed lens model, as was quantitatively demonstrated by Remolina González et al. (2021). We adopt the mass within the Einstein radius derived for SPT-CL J2011−5228 by Collett et al. (2017), $M(<\theta_E) = 1.6\times10^{14}\,M_\odot$. For SPT-CL J0356−5337, Mahler et al. (2020) report an Einstein radius $\theta_E = 14''$ for a source at $z = 3$, derived from their best-fit lens model. This translates to $M(<14'') = 8.6\pm0.9\times10^{13}\,M_\odot$, assuming 10% uncertainty. For IDCS J1426.5+3508, Gonzalez et al. (2012) report an arc radius of $\theta_E = 14.''2\pm0.''2$ and calculate a lower limit for the mass within the Einstein radius of $M(<\theta_E) = 6.9\pm0.3\times10^{13}\,M_\odot$, after accounting for the unknown redshift of the arc, and correcting for the overestimate associated

with this method, which they estimated to be a factor of 1.6. For the two remaining clusters, SPT-CL J0546−5345 and SPT-CL J0205−5829, we measured the arc distance using archival HST data from programs GO-12477 and GO-15294. We reduced the data following the same process as described in Section 2, and inspected the multiband imaging (F160W, F814W, and F606W) for lensing evidence. We find that the prominent arc in SPT-CL J0205−5829 is projected $20'' \pm 1''$ from the BCG. The HST data of SPT-CL J0546−5345 reveal several arc candidates, one of which was visible in ground-based data (Staniszewski et al. 2009). The geometry of this arc indicates that it is associated with a massive substructure in the western part of the cluster core, and may not be indicative of the mass of the primary cluster core. We therefore opted to use for our analysis the arc with the largest radius that is not likely to be tracing that structure, at a distance of $23\farcs5 \pm 1''$ northwest of the BCG. A third prominent arc appears in the near-infrared (F160W) $14''$ northeast of the BCG. None of the arcs in these two clusters have a known spectroscopic redshift measurement in the literature. We calculated the mass within the Einstein radii of these two clusters using the equation in Section 4, for two source redshifts spanning the reasonable redshift range for sources to be lensed and visible in the available data, $z_{\rm arc} = 3$ and 6. We applied the quadratic empirical correction from Remolina González et al. (2020) to obtain the corrected masses and their associated uncertainties here: $M_{\rm corr}(<\theta_{\rm E}) = (1.6 \pm 0.3 - 2.7 \pm 0.5) \times 10^{14}\, M_\odot$ and $M_{\rm corr}(<\theta_{\rm E}) = (1.4 \pm 0.2 - 3.1 \pm 0.5) \times 10^{14}\, M_\odot$ for SPT-CL J0546−5345 and SPT-CL J0205−5829, respectively.

To summarize, the core masses of the five strong lensing clusters at $z > 1$ range between $\sim$0.7–$1.6 \times 10^{14}\, M_\odot$. The lensing cluster COOL J1241 has a significantly smaller Einstein radius and enclosed mass than other strong lensing clusters at its redshift, $M(<5\farcs77) = 1.079^{+0.023}_{-0.007} \times 10^{13} M_\odot$. This result is consistent with our expectations from the different discovery methods of these clusters. The SPT clusters were detected due to their deep potential well that is responsible for the SZ signal, while COOL J1241 was discovered due to the presence of the giant arc irrespective of its cluster mass. While the core of the cluster is consistent with it being a low-mass galaxy cluster or group, the small Einstein radius and corresponding enclosed mass could alternatively be due to a diffuse mass distribution with low concentration.

Finally, we note that while not advisable, a measurement of the mass out to large radii of a few hundred kiloparsecs is technically possible since the mass reconstruction uses a parameterized lens modeling algorithm that assumes a functional form for the cluster halo. The extrapolation of the projected mass density to 500 kpc from the BCG results in $M(<500\ {\rm kpc}) = 3.6^{+0.8}_{-0.4} \times 10^{14} M_\odot$. We remind the reader that since the lensing evidence all falls within $\sim$50 kpc of our BCG, it cannot constrain the outskirts of the mass distribution; in fact it is common practice to fix the truncation parameter ($r_{\rm cut}$) of the cluster halo in the lens modeling process for that reason. To gain a better understanding of the statistical uncertainties of the lens model, we reran the lens model with $r_{\rm cut}$ free, with a prior of $250 < r_{\rm cut} < 1500$ kpc. The results of the free truncation model are consistent with the fiducial lens model. In particular, the mass within the strong lensing regime, where strong lensing evidence is observed, was unaffected. The statistical spread of the projected mass density increased by $\sim$50% and the lower limit reduced to $\sim 2.5 \times 10^{14}\, M_\odot$, but it is likely still an underestimate of the true uncertainty.

5.3. Revised Source Properties

In this section, we use our improved strong lensing model to update the source galaxy measurements of K21 that depend on lensing magnification: luminosity, SFR, and stellar mass ($M_\star$). Other results from K21 that are magnification independent remain unchanged, e.g., metallicity, dust extinction, and specific SFR. K21 used `galfit` modeling to measure the multiband photometry of the giant arc, and a `PROSPECTOR` SED-fitting analysis to determine the physical properties of the source. They reported an observed (i.e., before any magnification correction) SFR ${\rm SFR}_{0-50\ {\rm Myr}} = 913^{+380}_{-280} M_\odot\ {\rm yr}^{-1}$ and stellar mass $\log(M_\star/M_\odot) = 11.63^{+0.19}_{-0.24}$. We followed the methodology described in K21 to correct these measurements by the lensing magnification, as follows. For each measurement, we drew a random value from its posterior distribution function and divided it by a random value drawn from the distribution of average arc magnifications. We repeated this process 10,000 times to obtain a statistical sampling and derived the magnification-corrected source property and its uncertainties from the resulting combined distribution. The values that we report are the medians of these 10,000 samples with errors given by the difference between that and the 16th or 84th percentile values. To verify that our methodology is consistent with K21, we applied their magnification to their SED results and confirmed that we recover their demagnified results.

We then corrected the observed SFR and $M_\star$ for the magnification, in two ways. First, as was done in K21, we correct the values by the average magnification of the giant arc (see Section 4). Applying our magnification, $\langle \mu_{\rm arc} \rangle = 76^{+40}_{-20}$, to the SED results, we obtain magnification-corrected values of $\log(M_\star/M_\odot) = 9.8 \pm 0.3$ and ${\rm SFR} = 11.4^{+7.4}_{-5.9}\ M_\odot\ {\rm yr}^{-1}$. Our stellar mass and SFR estimates are about 2.4 times smaller than the ones found in K21 ($\log(M_\star/M_\odot) = 10.11^{+0.21}_{-0.26}$ and ${\rm SFR} = 27^{+13}_{-9} M_\odot\ {\rm yr}^{-1}$, respectively), using the same approach. Similarly, the luminosity should be updated by the ratio of the magnifications, or a $\sim$0.92 mag change in the absolute magnitude previously reported, to $M_{\rm UV} = -21.28 \pm 0.2$. The reason for this discrepancy comes from the revised magnification (Section 5.1), which scales directly with luminosity, stellar mass, and SFR.

Second, we corrected the observed SFR and $M_\star$ by the flux-weighted magnification of the arc. The proximity of the giant arc to the critical curve complicates this measurement directly from the arc, as areas with high flux occur near the critical curve where the magnification and its uncertainties are high. Instead, we take advantage of the relatively uniform magnification of the counterimage, which is not bisected by a critical curve, and thus its flux-weighted magnification is approximately the same as its average magnification. The flux ratio between the giant arc and its counterimage is the average flux-weighted magnification ratio. We proceeded as described below to obtain the flux ratio f, and then calculated the flux-weighted magnification of the giant arc as $\langle \mu_{c.i.} \rangle \times f$.

The total observed flux of the arc and the counterimage were measured from the HST F814W data. Since lensing is wavelength invariant, the flux ratio should not depend on the filter choice, but at the wavelength of the F814W image the counterimage is less contaminated by the BCG. We make use of detailed `galfit` modeling of the field that will be presented in a forthcoming paper by I. Sierra et al. (2024, in preparation) and refer the reader to that paper for details of the `galfit`

modeling. In short, light sources in a field of view of $10\farcs6 \times 9\farcs1$ enclosing the arc and the counterimage were modeled as two-dimensional Sérsic components, adding components iteratively to the model until the residuals between the data and model were consistent with the noise level. The resulting scene decomposition allowed us to disentangle the arc and the counterimage from contamination from foreground sources (e.g., the BCG light, and a blue source near constraint X1). The flux ratio between the giant arc and the counterimage is $f = 14 \pm 0.9$; the resulting flux-weighted magnification of the giant arc is $\langle \mu_{\rm arc,w} \rangle = 92^{+37}_{-31}$. Correcting the SFR and $M_\star$ by the flux-weighted magnification of the arc, we obtain $\mathrm{SFR} = 10.3^{+7.0}_{-4.4}\ M_\odot\,\mathrm{yr}^{-1}$ and $\log(M_\star/M_\odot) = 9.7 \pm 0.3$, 2.6 and 2.8 times smaller than previously reported by K21, respectively.

A revised measurement of the arc SED is beyond the scope of this paper. The shallow, four-band HST imaging provides superior resolution to the ground-based data, and a `galfit` analysis of these data will be presented elsewhere (I. Sierra et al. 2024, in preparation). In future work, we will combine the multiband HST imaging described here with forthcoming JWST imaging and spectroscopy to obtain a clump-by-clump analysis of the lensed source. This future analysis will significantly supersede an HST + ground-based measurement of the arc as a whole, as it will extend farther into the IR, and with greater depth and resolution.

As observed by K21, the magnification-corrected stellar mass and SFR places COOL J1241 within the range of other $4 \leqslant z < 6$ galaxies from the Santini et al. (2017) analysis of four Hubble Frontier Fields. Santini et al. (2017) measured the slope and intercept between stellar mass and SFR in log–log space, in different redshift bins. They used 2σ clipping to exclude outliers, and a Monte Carlo simulation to correct for Eddington bias. Applying Equation (1) from Santini et al. (2017) to the measured mass of COOL J1241 gives a predicted main-sequence (MS) SFR of $\log(\mathrm{SFR})_{\rm MS} = 2.06 \pm 0.13$. Our measured SFR is 5σ below the Eddington bias-corrected MS for $5 \leqslant z < 6$, although it falls within 1σ of the MS in the $4 \leqslant z < 5$ bin. Since COOL J1241 falls below the MS, it is consistent with a galaxy that has low levels of star formation relative to star formation MS galaxies at $z = 5$, although whether it is consistent with a poststarbust/quiescent galaxy remains to be seen (with JWST/NIRSpec observations). Further studies imply that higher stellar mass galaxies which fall below the MS experience sudden quenching by active galactic nucleus (AGN) feedback while lower stellar mass galaxies experience a slow decrease in SFR due to gas exhaustion (Man et al. 2016; Mancuso et al. 2016). Because COOL J1241 falls in the typical stellar mass range for galaxies at $5 \leqslant z < 6$, it is hard to predict which of these, if either, occurred. This invites a series of questions: did COOL J1241 ever look like the dust-enshrouded early star-forming galaxies? Is AGN feedback responsible for the lack of dust in the galaxy or is there evidence of gas exhaustion? Is the clumpiness that we observe the result of a merger or another process? Is there other evidence to suggest AGN feedback? While these answers are outside of the scope of this paper, our reported magnification values and deflection maps facilitate further investigation of these questions. Our analysis of COOL J1241 is an important stepping stone for analyzing a galaxy observed close to the edge of the Epoch of Reionization.

6. Summary and Future Work

We used shallow, multiband HST imaging to revise the lens model of COOL J1241, a system with a $z = 5.043$ galaxy lensed by a $z = 1.001$ cluster into a bright giant arc, first discovered by K21. The high spatial resolution data reveal the clumpiness of the arc, enabling detailed lens modeling of the system for the first time. We confirm the candidate counterimage identified by K21, and concur with their interpretation that the brightest clump on the arc is a result of high magnification under the critical curve. Other assumptions on the lensing configuration from the ground-based analysis, namely that the giant arc is formed by a common three-image arc configuration, appear to be inconsistent with the HST data. From the revised lensing analysis, we report the following.

1. We measure a projected mass density enclosed within the Einstein radius of the lensing cluster ($\theta_{\rm E} = 5\farcs77$ for a source at $z = 5.043$) of $M(<5\farcs77) = 1.079^{+0.023}_{-0.007} \times 10^{13} M_\odot$, consistent with an analytical estimate assuming spherical symmetry (Section 4).
2. We compile information on Einstein radii and enclosed masses of the five other known strong lensing clusters at the same redshift range, either from the literature or estimate them directly from archival HST data. We find that the Einstein radius, as well as the enclosed mass of the COOL J1241 cluster lens, are significantly lower than other known lensing clusters at $z \gtrsim 1$.
3. We measure an average magnification of $\langle \mu_{\rm arc} \rangle = 76^{+40}_{-20}$ for the giant arc and $\langle \mu_{c.i.} \rangle = 6.6^{+2.6}_{-2.2}$ for the counterimage, about a factor of $2.4^{+1.4}_{-0.7}$ higher than in the previous analysis of K21.
4. We measure the flux-weighted average magnification of the giant arc from the observed flux ratio between the arc and its counterimage, finding $\langle \mu_{\rm arc,w} \rangle = 92^{+37}_{-31}$.
5. We revise the magnification-dependent measurements of K21 to account for the higher magnification, by sampling from their `PROSPECTOR` SED analysis posterior distribution function and dividing by the flux-weighted lensing magnification. We obtain magnification-corrected values of $\log(M_\star/M_\odot) = 9.7 \pm 0.3$ and $\mathrm{SFR} = 10.3^{+7.0}_{-4.4}\, M_\odot\,\mathrm{yr}^{-1}$. The luminosity is similarly reduced by the ratio of magnifications, resulting in an absolute magnitude of $M_{\rm UV} = -21.28 \pm 0.2$.
6. The stellar mass and SFR of the lensed galaxy are within the range of other $5 \leqslant z < 6$ galaxies observed in the Hubble Frontier Fields (Santini et al. 2017), falling significantly below the $\log(\mathrm{SFR}) - \log(M_\star)$ MS (corrected for Eddington bias; Santini et al. 2017).

Imaging and spectroscopy of COOL J1241 with JWST (Cycle 1 program ID 2566, PI Khullar; Khullar et al. 2021a) will be combined with the shallow multiband HST data presented in this work (HST Cycle 28 GO-16484, PI Stark; Stark et al. 2020) to analyze the lensed galaxy fully on a clump-by-clump basis. These data will also enable a high-fidelity measurement of the giant arc and galaxy as a whole, after folding in our new and improved understanding of the lensing configuration of the giant arc. In future work, we will revise and improve the lens model by identifying and refining our lensing constraints using the JWST data. We expect that the wider wavelength range will bring out color information to which the HST filters are not sensitive.

Acknowledgments

This work is based on observations made with the NASA/ESA Hubble Space Telescope, obtained at the Space Telescope Science Institute, which is operated by the Association of Universities for Research in Astronomy, Inc., under NASA contract NAS 5-26555. These observations are associated with program GO-16484. This work also used archival HST data from programs GO-12477 and GO-15294. The HST data presented in this article were obtained from the Mikulski Archive at the Space Telescope Science Institute (MAST). The specific observations analyzed can be accessed via doi:10.17909/vk63-hb31. Support for HST program GO-16484 was provided through a grant from the STScI under NASA contract NAS 5-26555. This work used the MATLAB Astronomy and Astrophysics Toolbox (MAAT; Ofek 2014).

Facility: HST (ACS, WFC3).

Software: Source Extractor (Bertin & Arnouts 1996), `Lenstool` (Jullo et al. 2007), DrizzlePac (STSCI Development Team 2012), and MAAT (Ofek 2014).

ORCID iDs

Maxwell Klein https://orcid.org/0000-0001-5786-1272
Keren Sharon https://orcid.org/0000-0002-7559-0864
Kate Napier https://orcid.org/0000-0003-4470-1696
Michael D. Gladders https://orcid.org/0000-0003-1370-5010
Gourav Khullar https://orcid.org/0000-0002-3475-7648
Matthew Bayliss https://orcid.org/0000-0003-1074-4807
Håkon Dahle https://orcid.org/0000-0003-2200-5606
M. Riley Owens https://orcid.org/0000-0002-2862-307X
Antony Stark https://orcid.org/0000-0002-2718-9996
Sasha Brownsberger https://orcid.org/0000-0002-5430-4355
Keunho J. Kim https://orcid.org/0000-0001-6505-0293
Nicole Kuchta https://orcid.org/0000-0002-7072-7622
Guillaume Mahler https://orcid.org/0000-0003-3266-2001
Grace Smith https://orcid.org/0000-0003-3971-5727
Ryan Walker https://orcid.org/0000-0001-5424-3698
Katya Gozman https://orcid.org/0000-0003-2294-4187
Michael N. Martinez https://orcid.org/0000-0002-8397-8412
Owen S. Matthews Acuña https://orcid.org/0000-0001-9225-972X
Kaiya Merz https://orcid.org/0000-0001-5931-5056
Jorge A. Sanchez https://orcid.org/0000-0002-9142-6378
Daniel J. Kavin Stein https://orcid.org/0000-0001-8008-7270
Ezra O. Sukay https://orcid.org/0000-0002-1106-4881
Kiyan Tavangar https://orcid.org/0000-0001-6584-6144

References

Ahumada, R., Prieto, C. A., Almeida, A., et al. 2020, ApJS, 249, 3
Andersson, K., Benson, B. A., Ade, P. A. R., et al. 2011, ApJ, 738, 48
Bayliss, M. B., Hennawi, J. F., Gladders, M. D., et al. 2011, ApJS, 193, 8
Bellagamba, F., Tessore, N., & Metcalf, R. B. 2017, MNRAS, 464, 4823
Bertin, E., & Arnouts, S. 1996, A&AS, 117, 393
Bleem, L. E., Stalder, B., de Haan, T., et al. 2015, ApJS, 216, 27
Bocquet, S., Dietrich, J. P., Schrabback, T., et al. 2019, ApJ, 878, 55
Brodwin, M., Gonzalez, A. H., Stanford, S. A., et al. 2012, ApJ, 753, 162
Brodwin, M., Ruel, J., Ade, P. A. R., et al. 2010, ApJ, 721, 90
Casey, C. M., Zavala, J. A., Aravena, M., et al. 2019, ApJ, 887, 55
Claeyssens, A., Adamo, A., Richard, J., et al. 2023, MNRAS, 520, 2180
Collett, T. E., Buckley-Geer, E., Lin, H., et al. 2017, ApJ, 843, 148
Cornachione, M. A., Bolton, A. S., Shu, Y., et al. 2018, ApJ, 853, 148
Diego, J. M., Pascale, M., Kavanagh, B. J., et al. 2022, A&A, 665, A134
Elíasdóttir, Á., Limousin, M., Richard, J., et al. 2007, arXiv:0710.5636
Fan, X., Strauss, M. A., Becker, R. H., et al. 2006, AJ, 132, 117
Franx, M., Illingworth, G. D., Kelson, D. D., van Dokkum, P. G., & Tran, K.-V. 1997, ApJL, 486, L75
Frye, B., Broadhurst, T., & Benitez, N. 2002, ApJ, 568, 558
Gladders, M. D., & Yee, H. K. C. 2000, AJ, 120, 2148
Gladders, M. D., Yee, H. K. C., & Ellingson, E. 2002, AJ, 123, 1
Gnedin, N. Y., & Madau, P. 2022, LRCA, 8, 3
Gonzalez, A. H., Stanford, S. A., Brodwin, M., et al. 2012, ApJ, 753, 163
Johnson, T. L., Rigby, J. R., Sharon, K., et al. 2017a, ApJL, 843, L21
Johnson, T. L., & Sharon, K. 2016, ApJ, 832, 82
Johnson, T. L., Sharon, K., Gladders, M. D., et al. 2017b, ApJ, 843, 78
Jullo, E., Kneib, J.-P., Limousin, M., et al. 2007, NJPh, 9, 447
Khullar, G., Bayliss, M., Brownsberger, S., et al. 2021a, Characterizing Stellar Mass Assembly and Physical Properties in the Brightest Galaxy in the Redshift>5 Universe JWST Proposal, Cycle 1, ID., Baltimore, MD: STScI, #2566
Khullar, G., Gozman, K., Lin, J. J., et al. 2021b, ApJ, 906, 107
Kneib, J.-P., & Natarajan, P. 2011, A&ARv, 19, 47
Kubo, J. M., Allam, S. S., Drabek, E., et al. 2010, ApJL, 724, L137
Limousin, M., Kneib, J.-P., & Natarajan, P. 2005, MNRAS, 356, 309
Mahler, G., Sharon, K., Gladders, M. D., et al. 2020, ApJ, 894, 150
Man, A. W. S., Greve, T. R., Toft, S., et al. 2016, ApJ, 820, 11
Mancuso, C., Lapi, A., Shi, J., et al. 2016, ApJ, 833, 152
Meena, A. K., Zitrin, A., Jiménez-Teja, Y., et al. 2023, ApJL, 944, L6
Mowla, L., Iyer, K. G., Desprez, G., et al. 2022, ApJL, 937, L35
Ofek, E. O. 2014, MAAT: MATLAB Astronomy and Astrophysics Toolbox, Astrophysics Source Code Library, ascl:1407.005
Persson, S. E., Barkhouser, R., Birk, C., et al. 2008, Proc. SPIE, 7014, 70142V
Reichardt, C. L., Stalder, B., Bleem, L. E., et al. 2013, ApJ, 763, 127
Remolina González, J. D., Sharon, K., Mahler, G., et al. 2021, ApJ, 920, 98
Remolina González, J. D., Sharon, K., Reed, B., et al. 2020, ApJ, 902, 44
Robertson, B. E. 2022, ARA&A, 60, 121
Santini, P., Fontana, A., Castellano, M., et al. 2017, ApJ, 847, 76
Sharon, K., Bayliss, M. B., Dahle, H., et al. 2020, ApJS, 247, 12
Sharon, K., Gladders, M. D., Rigby, J. R., et al. 2012, ApJ, 746, 161
Soifer, B. T., Neugebauer, G., Franx, M., Matthews, K., & Illingworth, G. D. 1998, ApJL, 501, L171
Stalder, B., Ruel, J., Šuhada, R., et al. 2013, ApJ, 763, 93
Stalder, B., Stark, A. A., Amato, S. M., et al. 2014, Proc. SPIE, 9147, 91473Y
Stanford, S. A., Brodwin, M., Gonzalez, A. H., et al. 2012, ApJ, 753, 164
Staniszewski, Z., Ade, P. A. R., Aird, K. A., et al. 2009, ApJ, 701, 32
Stark, A. A., Bayliss, M., Brownsberger, S., Gladders, M. D., & Sharon, K. 2020, First Radio Observations of the Brightest Object at z >5 HST Proposal. Cycle 28, ID, #16484
Stark, D. P., Auger, M., Belokurov, V., et al. 2013, MNRAS, 436, 1040
STSCI Development Team, 2012 DrizzlePac: HST image software, Astrophysics Source Code Library, ascl:1212.011
Sukay, E., Khullar, G., Gladders, M. D., et al. 2022, ApJ, 940, 42
Vanzella, E., Claeyssens, A., Welch, B., et al. 2023, ApJ, 945, 53
Welch, B., Coe, D., Diego, J. M., et al. 2022a, Natur, 603, 815
Welch, B., Coe, D., Zackrisson, E., et al. 2022b, ApJL, 940, L1
Welch, B., Coe, D., Zitrin, A., et al. 2023, ApJ, 943, 2
Zhuang, Z., Leethochawalit, N., Kirby, E. N., et al. 2023, ApJ, 948, 132